DOI: 10.53469/jpce.2026.08(01).03

# Multi-objective Optimization of Passive Flexible Protection Network Layouts for Rockfall Hazards Based on Evolutionary Algorithms

**Jiayu Yan[1], Shengwu Qin[1,*], Yong Tao[2], Wendi Rao[2], Zhenmin Chen[1], Shuhao Dong[1]**

[1]College of Construction Engineering, Jilin University, Changchun 130061, Jilin, China
[2]Jilin Geological Environment Monitoring Center (Jilin Geological Disaster Emergency Technical Guidance Center), Changchun 130021, Jilin, China
*Correspondence Author, qinsw@jlu.edu.cn*

**Abstract:** ***Rockfall disasters pose a severe threat to infrastructure safety, and the rational design of passive flexible protection network layouts is critical for disaster mitigation. Taking the Guanmenla rockfall area in Ji'an City, Jilin Province as a case study, this paper develops an optimization framework for protection net placement by coupling rockfall numerical simulation with multi-objective evolutionary algorithms. Firstly, a three-dimensional rockfall motion model was established using the RAMMS software. Through 129,000 Monte Carlo simulations, the statistical distribution characteristics of key dynamic parameters—including rockfall trajectories, velocities, kinetic energy, and bounce heights—were obtained. Subsequently, a multi-objective optimization model aimed at maximizing the interception rate and minimizing engineering costs was constructed, with the Pareto optimal solution set solved via the NSGA-II algorithm. The results indicate that the 95th percentile bounce height along the road is 2.04 m, with kinetic energy ranging from 500 to 3200 KJ The optimized scheme adopts a zonal cascading protection strategy, incorporating a total of four flexible protection nets. This configuration achieves a total interception rate of 98.43% with a total engineering cost of 368,440 RMB. Verification through back-simulation in RAMMS demonstrated an error of less than 0.5%. This research establishes a systematic workflow from dynamic parameter extraction to scheme optimization and validation, providing a scientific basis for the design of rockfall protection engineering.***

**Keywords:** Rockfall, Passive flexible protection networks, NSGA-II, Multi-objective optimization**.**

## 1. Introduction

Rockfall is a typical slope-related geological hazard, characterized by the detachment of unstable rock masses from slopes under external forces, which subsequently roll, bounce, and collide until they finally accumulate at the slope toe (He et al., 2014). Such disasters are characterized by high frequency, complex triggering factors, wide spatial distribution, rapid onset, and severe destructiveness. Their high-velocity impact poses a significant threat to infrastructure at the slope toe, such as buildings and major transportation arteries. Furthermore, rockfalls can trigger secondary disasters, leading to large-scale ecological damage and socio-economic losses (Yu et al., 2020; Zhang, 1993; Zhang et al., 2004).

Regarding the prevention and control of rockfall hazards, existing technical measures can be classified into four categories: active slope stabilization, rigid passive protection, flexible passive protection, and auxiliary protective measures (Zhang et al., 2021). Among these, passive flexible protection networks dissipate rockfall kinetic energy through large geometric nonlinear deformations of the structure and significant slippage between components. Due to their adaptability to complex terrain, high energy-absorption capacity, cost-effectiveness, and short construction periods, they have increasingly become the mainstream choice for rockfall disaster mitigation (Zhao et al., 2023).

With the advancement of computational technology, numerical simulation has become an essential tool for rockfall motion analysis. Simulation methods are generally divided into two-dimensional (2D) and three-dimensional (3D) approaches (NanYa et al., 1996). 2D methods, typically based on the lumped-mass model (e.g., RocFall software), often lead to biased results due to the neglect of lateral movement (Liu, 2012). D methods are more consistent with real-world conditions; for instance, RocPro3D employs a probabilistic rigid-body approach, while the Discrete Element Method (DEM) calculates force transmission between particles through contact mechanics models (Sarro et al., 2014). The RAMMS software, jointly developed by ETH Zurich and the WSL Institute, utilizes a non-smooth contact dynamics algorithm based on hard contact laws. Unlike traditional restitution coefficient methods, RAMMS assumes that rock-ground interactions are primarily governed by frictional dissipation mechanisms, allowing for a more natural simulation of transitions between motion modes such as bouncing, rolling, and sliding (Yang et al., 2023).

In terms of protection system research, (Gottardi & Govoni, 2010) conducted full-scale impact tests ranging from500kJ to 5000 kJ verifying the interception capacity of flexible nets. (Zhao et al., 2013) revealed the three-stage dynamic response characteristics of these systems through 11 sets of full-scale tests. Given the high cost and limited data of field trials, researchers have turned to numerical simulation. (Fu, 2021) proposed a collaborative active-passive protection scheme based on Rockfall software, (Zhong, 2021) analyzed the dynamic response of networks to optimize structural design. (Zhou et al., 2012) found that the deformation and peak impact force of flexible nets are linearly related to impact velocity and rock size, noting that small-sized rocks tend to create a "bullet effect," penetrating the protection net.

However, existing research exhibits a gap in the systematic integration of rockfall kinematic characteristics and the scientific design of protection networks. In engineering

practice, parameters and layouts of protection nets are often determined based on empirical judgment or simplified 2D calculations. This semi-empirical approach frequently leads to insufficient protective capacity, resulting in structural failure and recurring disasters. Although numerical simulations can accurately predict rockfall trajectories and dynamic parameters, there is a lack of a systematic optimization framework that comprehensively considers multiple objectives such as interception efficiency, energy dissipation, and cost.

Therefore, taking the Guanmenla rockfall area in Ji'an City, Jilin Province as a case study, this paper constructs a design framework for protection net layouts by integrating rockfall numerical simulation with multi-objective optimization algorithms. First, a 3D rockfall motion model is established using the RAMMS platform to reveal motion patterns and extract key dynamic parameters, including trajectories, velocities, kinetic energy, and bounce heights. Subsequently, a multi-objective optimization model for passive flexible protection net placement is constructed to maximize interception rates and energy dissipation efficiency while minimizing costs. The layout scheme is then optimized using the NSGA-II algorithm and validated through numerical simulation. Through this approach, this study establishes an integrated optimization framework coupling numerical simulation with evolutionary algorithms, achieving a systematic workflow from dynamic parameter extraction to optimization validation, thereby providing a scientific basis for the design of protection networks.

## 2. Study Area

The study area is located in Ji'an City, southeastern Jilin Province, China, under the jurisdiction of Tonghua City. The region is bounded by longitudes 125°34′E to 126°02′E and latitudes 40°52′N to 41°35′N, encompassing a total area of 3,341 km². The Guanmenla rockfall site, the primary focus of this investigation, is situated in Yulin Town, approximately 30 km south of the Ji'an urban center. Notably, the hazard zone is immediately adjacent to National Highway G506, a critical transportation corridor linking Ji'an with townships along the Yalu River. This highway serves as a vital artery for regional freight, passenger transit, and cross-border tourism (Figure 1).

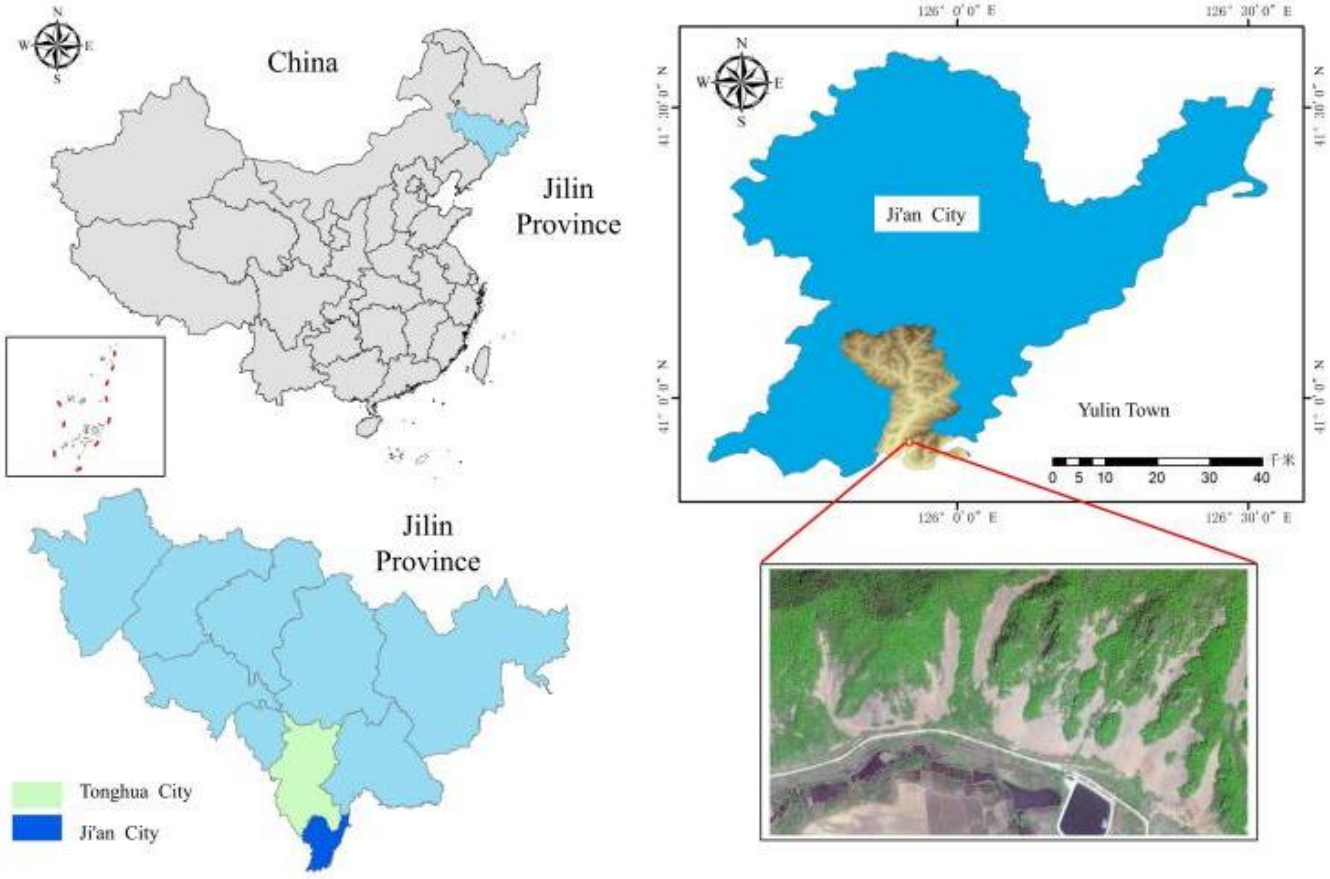


**Figure 1:** Location of the study area

The rockfall hazards in this region are driven by a synergy of anthropogenic and natural factors. Historical road construction, specifically slope-toe excavation, combined with intense precipitation during the summer monsoon, has triggered progressive rock mass deterioration and created over steepened slope configurations. Consequently, frequent rockfall events pose a persistent threat to vehicular and pedestrian safety along the highway corridor.

The collapse-prone slope exhibits the morphology of a high-steep rock cliff, trending northeast-southwest. It has a longitudinal extension of approximately 350 m and a transverse width of 200 m, covering an area of roughly 6.2 × $10^4$ m². Topographic surveys indicate that the slope crest reaches an elevation of 361 m above sea level, while the toe sits at 131 m, resulting in a maximum vertical relief of 230 m. The average slope gradient is approximately 52°, with

localized cliff sections reaching 70° to 85°, characterizing a typical high-steep slope system. The predominant slope aspect is 310° (northwest-facing), which is nearly perpendicular to the highway alignment. This geometric configuration creates unfavorable structural conditions; specifically, daylight-facing discontinuities facilitate toppling and planar failure mechanisms, directly endangering the underlying roadway infrastructure.

## 3. Materials and Methods

### 3.1 Numerical Simulation Method for Rockfall Movement

The RAMMS (Rapid Mass Movement Simulation) software, jointly developed by ETH Zurich and the WSL Institute for Snow and Avalanche Research (https://ramms.ch/), is specifically designed to simulate the rigid-body motion characteristics of rockfalls. The software employs six primary state variables to describe the kinematic features of a rockfall: three translational velocity components and three rotational angular velocity components. Based on these variables, key parameters such as kinetic energy, trajectories, and bounce heights can be calculated. Crucially, the orientation and rotational velocity of the rock are fully accounted for during the rock-ground interaction process (Kumar et al., 2024).

In contrast to the restitution coefficient methods adopted by most rockfall simulation programs, RAMMS introduces an innovative Non-smooth Contact Dynamics (NSCD) algorithm based on the Hard Contact Law. This approach posits that rock-ground interactions are not solely controlled by simple elastic rebounding mechanics; instead, the primary motion modes—bouncing, rolling, and sliding—are governed by frictional dissipation mechanisms during the contact process. This theoretical framework enables a more natural simulation of the transitions between motion modes, thereby avoiding the uncertainties associated with stochastically assigned rebound parameters in traditional methods (Li et al., 2021).

In RAMMS, the contact force is modeled as a hard unilateral constraint with Coulomb friction characteristics and is solved using non-smooth frictional contact dynamics. When the rock mass contacts the ground, the equation of motion is expressed as follows:

$$M\ddot{q} = F(q,\dot{q}) + G^T(q)\lambda$$

Where $M(q)$ is the mass matrix, $q$ and $\dot{q}$ epresent the generalized coordinates and generalized velocities, respectively; $F(q,\dot{q})$ is the external force vector (a function of rock position and velocity) including gravity and gyroscopic forces;$\lambda$ is the contact force vector, $G^T(q)$ is the transpose of the contact Jacobian, which defines the direction of the contact forces. Depending on the geometry of the rock mass at the contact point, multiple contact forces may be active simultaneously (Caviezel et al., 2021).

To detect the contact state between the rock mass and the rebounding surface, the contact point is simultaneously subjected to a normal contact force and a tangential frictional contact force. These forces are treated as constraint reaction forces that alter the rockfall's direction of motion. The contact state of the rigid rock mass is determined by continuously monitoring the normal gap between the rock's characteristic vertices and their corresponding projected points on the rebounding surface. The gap function is defined as:

$$g_n = (r_p - r_c) \cdot n$$

Where $r_p$ is the position vector of the projected point on the rebounding surface, $r_c$ is the position vector of the rock mass vertex, $n$ is the unit normal vector of the contact surface.

The criteria for determining contact conditions follow these rules: when $g_n > 0$, the rigid rock mass is separated from the ground, the contact force $\lambda_n = 0$, and the rock is in free flight. When $g_n \leq$, contact or penetration occurs, and the contact force must be calculated to prevent further penetration. The software allows for a minimum penetration depth to accurately assess contact states under complex topographic conditions (Lu et al., 2019).

The non-smooth contact dynamics approach in RAMMS offers several distinct advantages: Explicit Physical Mechanism: It circumvents the randomness inherent in empirical parameters like restitution coefficients. Natural Mode Transition: It seamlessly captures the transitions between rockfall motion modes (bouncing, rolling, and sliding). Complex Dissipation Modeling: It accounts for the intricate mechanisms of ground deformation and energy dissipation. It is highly applicable to complex terrains and diverse soil/rock material conditions. This software is particularly well-suited for research requiring precise simulation of rock-ground interaction mechanisms and engineering applications such as the structural load analysis of protective systems.

### 3.2 Mathematical Description of Multi-objective Optimization Problems

A Multi-Objective Optimization Problem (MOOP) refers to a mathematical programming problem that requires the simultaneous optimization of two or more objective functions. Such problems are prevalent in practical fields such as engineering design, resource allocation, and production scheduling. Unlike single-objective optimization, the various objectives in a MOOP are typically in conflict with one another. Consequently, it is often impossible to find a single solution that minimizes all objectives simultaneously; instead, the goal is to identify an optimal set of trade-offs between the competing objectives (Kumar et al., 2024).

The general mathematical form of a multi-objective optimization problem can be formulated as follows:

Objective Functions: $\mathrm{F(x)} = [\mathrm{f_1(x)}, \mathrm{f_2(x)}, \cdots, \mathrm{f_m(x)}]^{\mathrm{T}}$

Constraints: $\mathrm{g_i(x)} \leqslant 0, \mathrm{i} = 1,2,\cdots,\mathrm{p}$; $\mathrm{h_j(x)} = 0, \mathrm{j} = 1,2,\cdots,\mathrm{q}$; $\mathrm{x} \in \Omega$

Where $\mathbf{x} = [x_1, x_2, \cdots, x_n]^T$ is the n-dimensional decision variable vector, representing the design parameters to be determined. F(x) is the m-dimensional objective function vector, containing the m objectives to be optimized simultaneously. $g_i(\mathbf{x})$ and $h_j(\mathbf{x})$ represent the i-th inequality constraint and j-th equality constraint, respectively. Ω denotes the feasible region in the decision variable space, defined by

the collective constraints. Any x that satisfies all constraints is termed a feasible solution, and the set of all such solutions constitutes the feasible set. (Moral & Dulikravich, 2008).

Traditional approaches to solving MOOPs include the weighted sum method, the $\varepsilon$-constraint method, and goal programming. These methods typically convert the multi-objective problem into a single-objective one. However, they yield only one solution per run and require repeated iterations with adjusted parameters to obtain multiple trade-off options. With the development of evolutionary computation, population-based Multi-Objective Evolutionary Algorithms (MOEAs) have become the mainstream approach. MOEAs can obtain multiple, uniformly distributed Pareto optimal solutions in a single simulation run (Yannibelli & Amandi, 2013).

The mapping of the Pareto optimal set into the objective space is known as the Pareto Front $PF^*$:

$$PF^* = \{\mathbf{F}(\mathbf{x}^*) = [f_1(\mathbf{x}^*), f_2(\mathbf{x}^*), \cdots, f_m(\mathbf{x}^*)]^T | \mathbf{x}^* \in P^*\}$$

The Pareto front delineates the trade-off boundary between objective functions, intuitively illustrating the "cost" of improving one objective in terms of the degradation of others. For a bi-objective minimization problem, the Pareto front typically appears as a downward-sloping curve or polyline in the objective space, moving from the upper-left to the lower-right. (Development of Parallel Multiobjective Genetic Algorithm for Designing Flexible Systems-All Databases, n.d.).

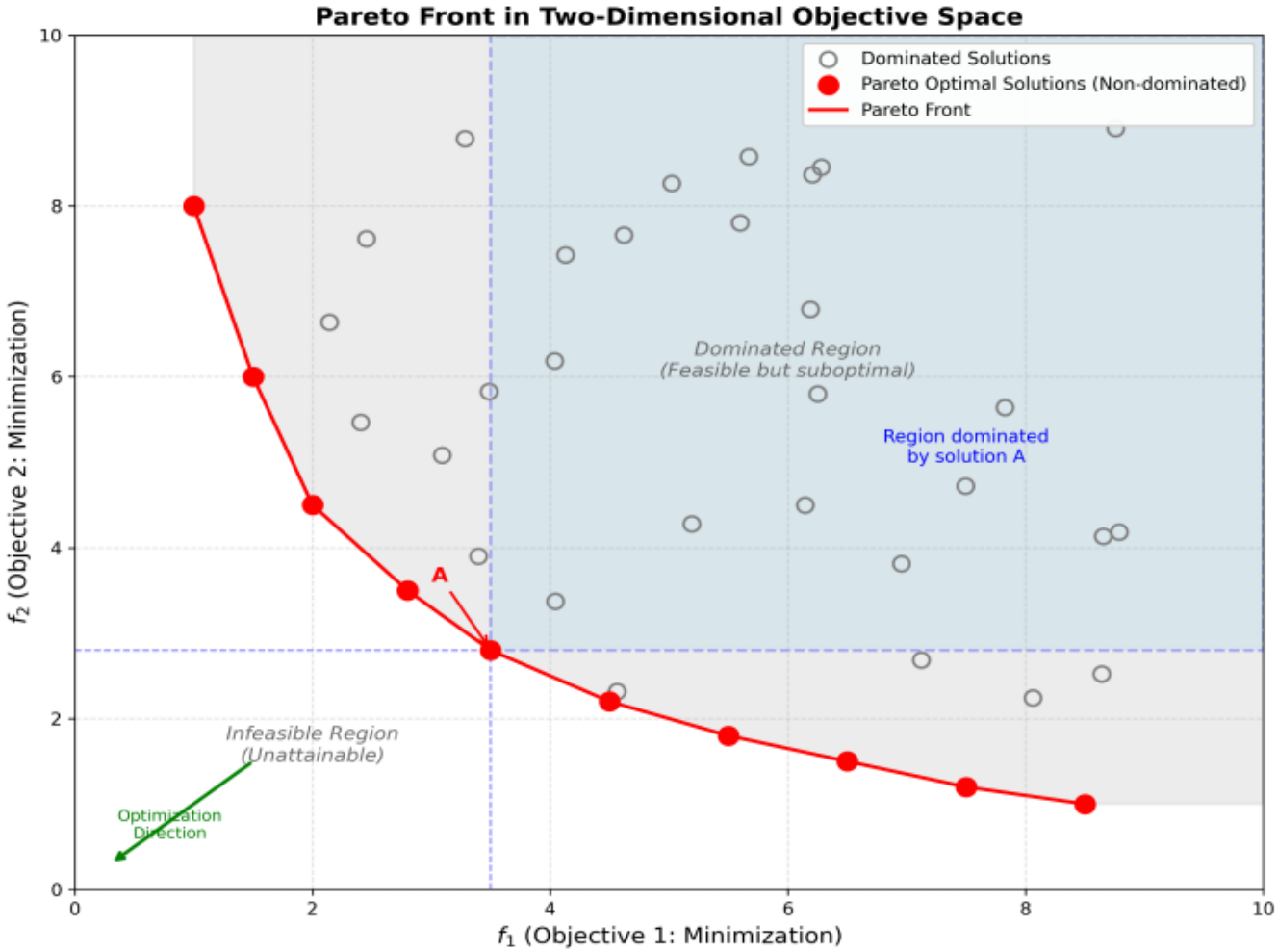


**Figure 2:** Schematic diagram of the Pareto front in the two-dimensional target space

### 3.3 Analysis of the Multi-objective Characteristics of Guard Net Layout Issues

The optimization of protection network layouts is fundamentally a trade-off between two competing objectives: maximizing the rockfall interception rate and minimizing the associated engineering construction costs. A profound conflict exists between these goals, as the primary mechanisms for enhancing interception efficiency—such as increasing the spatial coverage of nets, elevating net heights to capture high-trajectory boulders, and deploying higher energy-rated components—inevitably lead to a substantial escalation in capital expenditure (Volkwein et al., 2011). Conversely, any attempt to curtail costs by reducing the number of structures or lowering their technical specifications directly compromises the system's capacity to mitigate high-energy impacts, potentially resulting in structural failure or bypass events. Consequently, the core of the engineering challenge lies in identifying a rational equilibrium between safety performance and budgetary constraints.

The essence of this conflict lies in the divergent response directions of the interception rate and cost relative to the configuration parameters. Let $w$ represent the integrated configuration level of the protection network (a composite manifestation of quantity, height, and energy capacity). The

interception rate $R(w)$ typically increases monotonically with $w$, as does the engineering cost $C(w)$. Consequently, there is no single configuration level $w^*$ that simultaneously maximizes $R(w)$ and minimizes $C(w)$ (Ferrari et al., 2016). This inherent lack of a single optimal solution necessitates the application of Pareto optimization methods, which are particularly suited for problems characterized by conflicting objectives, mixed-integer decision variables, and non-convex feasible regions.

Furthermore, employing a Pareto-dominant Multi-Objective Evolutionary Algorithm (MOEA) to address this layout problem provides several distinct advantages over traditional optimization techniques. Primarily, MOEAs are capable of generating a uniformly distributed set of Pareto optimal solutions within a single computational execution, thereby providing a comprehensive mapping of the trade-off landscape between safety and cost. This population-based search mechanism is exceptionally robust in navigating the complexities of mixed-integer variables and complex constraints, significantly reducing the risk of the model converging to local optima. Moreover, by bypassing the requirement to pre-assign subjective weight coefficients to the objective functions, the algorithm ensures a more objective optimization process. This allows decision-makers to evaluate the entire set of non-dominated solutions and select a final configuration that aligns with the specific risk tolerance and financial conditions of the project. Additionally, the inherent scalability of the MOEA framework facilitates the seamless integration of further optimization objectives or site-specific constraints, making it a highly adaptable tool for complex geological engineering applications.

### 3.4 Principles and Implementation of NSGA-II Algorithm

The Non-dominated Sorting Genetic Algorithm II (NSGA-II), proposed by Deb et al. in 2002, serves as the computational engine for the multi-objective optimization in this study. As one of the most widely applied evolutionary algorithms in engineering, NSGA-II addresses the limitations of its predecessor by incorporating several critical innovations (Zhao et al., 2018). Most notably, the algorithm utilizes a fast non-dominated sorting strategy that reduces computational complexity from O(MN3) to O(MN2), where M is the number of objectives and N is the population size. Furthermore, the introduction of a crowding distance mechanism eliminates the need for user-defined sharing parameters, while the implementation of an elitist strategy ensures that superior individuals are preserved throughout the evolutionary process. These features collectively endow NSGA-II with exceptional convergence properties and the ability to maintain diverse solutions along the Pareto front (Zhang & Lu, 2021).

In addressing the continuous optimization problem of protection net placement, a real-number encoding scheme is adopted. Each individual's chromosome is represented by a $\mathbf{x} = [x_1, y_1, z_1, h_1, \cdots, x_n, y_n, z_n, h_n]$ , Where $(x_i, y_i, z_i)$ $i$ denotes the spatial coordinates of the i-th protection net, $h_i$ represents its corresponding height. The selection process employs a binary tournament strategy, which identifies superior candidates for the mating pool based on the crowding distance comparison operator. To explore the search space, Simulated Binary Crossover (SBX) is utilized, with the distribution of offspring around the parents controlled by a distribution index $\eta_c$. Local search and population diversity are further enhanced through polynomial mutation, which introduces random perturbations to gene values governed by a mutation distribution index $\eta_m$.

The specific parameter configuration for the algorithm was determined based on established literature and preliminary experimental results, as detailed in Table 1. A population size of 100 was selected to balance global search capability with computational efficiency, while the maximum number of generations was set to 300 to ensure sufficient convergence. The crossover probability was maintained at 0.9 to facilitate robust exploration, and the mutation probability was set to 1/16 to prevent premature convergence by maintaining genetic diversity. Standard values of 20 were assigned to the distribution indices for both SBX $\eta_m$ and polynomial mutation $\eta_c$, providing a stable distribution for offspring generation.

**Table 1:** Parameter Configuration of NSGA-II Algorithm

| Parameter | Symbol | Value | Basis |
|---|---|---|---|
| Population size | $N$ | 100 | Balancing search capability and computational efficiency |
| Maximum iterations | $T_{max}$ | 300 | Ensuring sufficient convergence of the algorithm |
| Crossover probability | $p_c$ | 0.9 | Guaranteeing robust global exploration capability |
| Mutation probability | $p_m$ | 1/16 | Maintaining population genetic diversity |
| SBX | $\eta_c$,$\eta_m$ | 20 | Adopting standard empirical values |

## 4. Results

### 4.1 Establishment of 3D Terrain Model

To obtain high-resolution imagery of the study area, this research utilized Unmanned Aerial Vehicle (UAV) photogrammetry. A multi-rotor UAV equipped with a high-precision camera was deployed to perform systematic aerial surveys, capturing a dense sequence of images that encompassed the entire rockfall site and its surrounding vicinity. Based on advanced image processing algorithms, feature point extraction, matching, and three-dimensional reconstruction were executed to generate a high-precision Digital Surface Model (DSM).

To account for the spatial distribution and physical extent of rockfall movement, regional optimization of the ground point model was performed. Initially, the boundaries of the potential rockfall impact zone were delineated within a Geographic Information System (GIS) platform. This delineation was based on topographic factors — including source area location, slope aspect, and gradient — supplemented by field investigations of historical rockfall distributions and kinematic characteristics. By integrating topographic constraints, gravitational orientation, and probable motion paths, the delineated boundary ensured comprehensive coverage of all potential impact zones. Subsequently, the 3D point cloud data underwent refined processing using specialized software suites, specifically Cloud Compare and LiDAR360, to enhance data quality.

Following these procedures, the optimized Triangulated

Irregular Network (TIN) model was converted into a regular grid-format Digital Elevation Model (DEM). The grid resolution was established at 0.5 m, providing an optimal balance between the topographic precision required for rockfall motion simulation and computational efficiency. During the DEM generation process, a rigorous quality control protocol was implemented; elevation statistical analysis and slope rationality checks were conducted to identify and rectify anomalous elevation values and data voids, thereby ensuring the continuity and integrity of the topographic model.

Ultimately, the refined DEM data were imported into the RAMMS software platform to construct a high-precision 3D terrain model tailored for numerical rockfall simulation. This model accurately reproduces the complex topographic relief, slope variations, and micro-geomorphic features of the study area. It serves as a robust foundational dataset for the subsequent simulation of rockfall trajectories, the analysis of velocity and kinetic energy evolution, and the systematic assessment of hazard zonation.

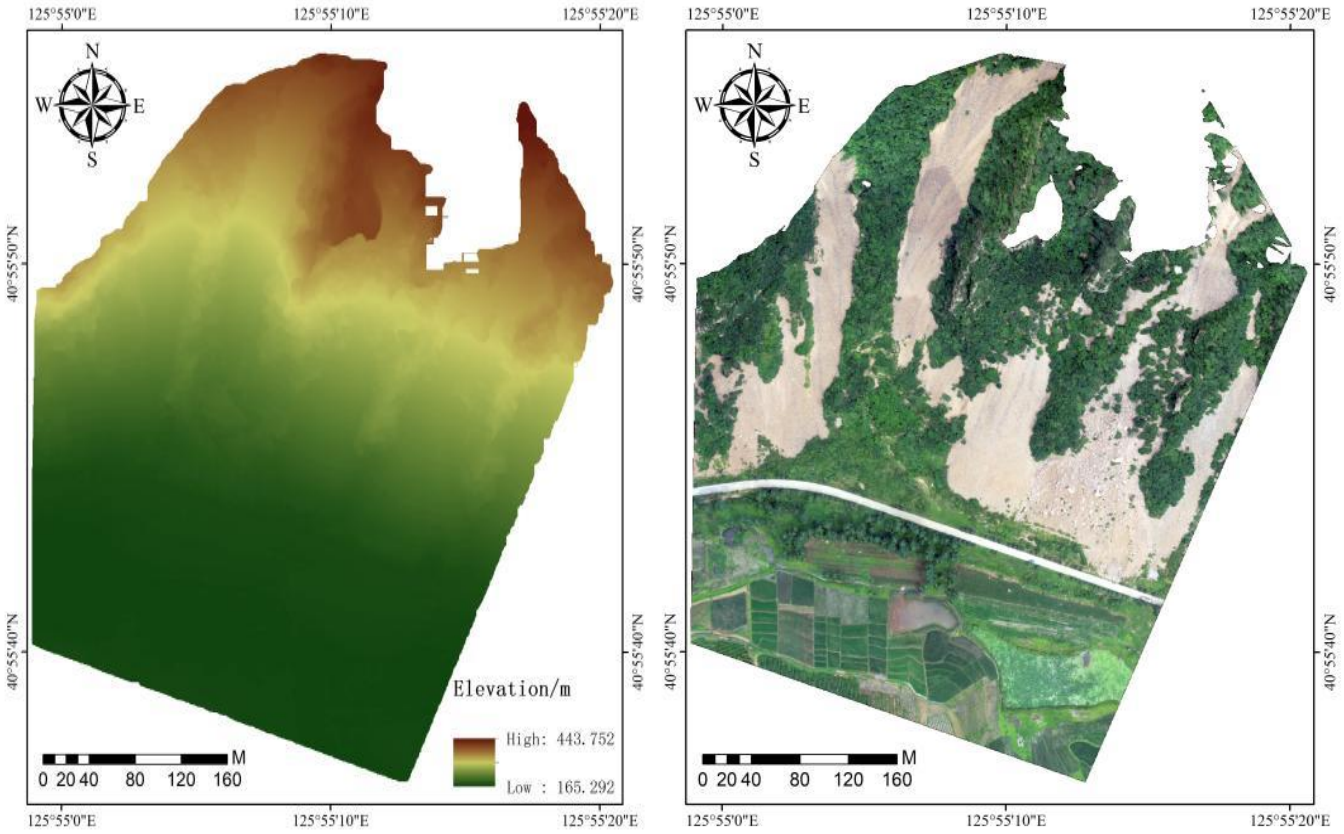


**Figure 3:** Digital elevation model and orthophoto of the study area

### 4.2 Setting of Rockfall Model Parameters

To precisely determine the geometric parameters required for the simulation, a multi-source data fusion approach was implemented. Initially, UAV oblique photogrammetry was employed to perform 3D scanning of the rockfall source areas and the boulders scattered across the slope, facilitating the acquisition of their spatial distribution and morphological characteristics. Furthermore, systematic field geological investigations were conducted to perform in-situ measurements and statistical analyses of the shapes, triaxial dimensions, and masses of representative rock blocks. By synthesizing the morphological statistics of historical rockfall samples, the predominant shape types and the characteristic size distribution patterns within the study area were effectively identified.

Based on these empirical datasets, geometric models of rock blocks reflecting the actual site conditions were established within the "Rock Builder" module of the RAMMS software. To account for the scale variations of unstable rock masses in the source area and the grain-size distribution of historical rockfalls, five distinct size classes of polyhedral rock models were constructed. The geometric configurations for each model were calibrated against the field-measured data, while the density parameters were assigned in accordance with the specific lithological characteristics of the site. The detailed parameter settings for these models are summarized in Table 2.

**Table 2:** Falling Rock Modeling Parameters of RAMMS ROCKFALL

| ID | Shape | Density kg/m$^3$ | Mass kg | Volume m$^3$ |
|---|---|---|---|---|
| 1 | Actual Morphology | 2700 | 21.5 | 0.008 |
| 2 | Actual Morphology | 2700 | 172.8 | 0.064 |
| 3 | Actual Morphology | 2700 | 926.4 | 0.343 |
| 4 | Actual Morphology | 2700 | 2703.2 | 1.0 |
| 5 | Actual Morphology | 2700 | 5381.72 | 2.0 |

### 4.3 Calibration and Validation of Key Parameters

The RAMMS software incorporates a comprehensive terrain classification system derived from extensive field rockfall experiments and comparative laboratory simulations. This system pre-defines 13 selectable terrain categories (Table 3), encompassing common geomorphic units such as bedrock,

scree slopes, soil-covered surfaces, and vegetated areas. The user manual provides illustrative examples and selection methodologies for each category, alongside recommended values for slope mechanical parameters, enabling users to assign appropriate terrain characteristics based on site-specific geological conditions.

**Table 3:** Terrain Category and Friction Parameter Default Values of RAMMS ROCKFALL

| Terrain Category | Example | $M_E$ (Mpa) | $C_d$ |
|---|---|---|---|
| River / Swamp | Marsh, grassland, hydromorphic soil | 0.2 | 1000 |
| Topsoil | Meadow, steppe | 3 | 1.55 |
| Deep soil | Unpaved mountain roads, alpine meadow | 4 | 1.8 |
| Forest | Forested areas | 5.5 | 1.2 |
| Vegetated scree | Small-grained scree with good vegetation cover | 6 | 2.1 |
| Fine scree | Pebbles (unvegetated), d≤5cm, $d_{50}$≤5cm | 7 | 2.3 |
| Medium scree | Unvegetated, d≤20cm, $d_{50}$≤10cm | 10 | 2.7 |
| Coarse scree | Unvegetated, d≤50cm, $d_{50}$≤30cm | 15 | 3.5 |
| Large blocks | Boulders / Talus | 20 | 3.5 |
| Mountain road | Mountainous roads | 50 | 2 |
| Asphalt road | Asphalted surfaces | 75 | 2 |
| Bedrock | Outcropping rock, cliffs | 100 | 4 |
| Snow | Accumulated snow | 0.1 | 1 |

In the RAMMS model, two pivotal parameters—ground strength (ME) and the drag coefficient (Cd) —significantly influence energy dissipation during rockfall motion. ME, expressed as a modulus of elasticity in units of Mpa, is a geotechnical parameter describing the deformation characteristics of the surface material. It characterizes the pressure required to achieve a specific strain or settlement within a given soil layer. A higher ME value indicates greater ground stiffness, resulting in shallower indentations upon impact and, consequently, lower energy dissipation during rock-ground interactions. In essence, ground stiffness increases proportionally with ME, with hard bedrock exhibiting significantly higher values than loose, unconsolidated soil. Complementarily, the drag coefficient Cd governs the magnitude of viscous resistance experienced by the rock during contact. A higher Cdvalue exerts a stronger retarding effect as the rock moves across the surface, leading to greater energy dissipation. This coefficient primarily reflects the influence of the viscoplastic properties and surface roughness of the terrain on the kinematic evolution of the rockfall.

For this investigation, a systematic parameter calibration was performed based on the environmental characteristics of the unstable rock mass. The bedrock in the study area consists primarily of gneiss, while land-use types on the slope include forest and agricultural land. By integrating detailed field geological survey results with the material composition and surface features of different geomorphic units, a localized terrain classification scheme was established. Specifically, the weathered rock cliffs in the rockfall source area were classified as Bedrock; the areas covered by slope wash and residual deposits were designated as Fine scree; and the residential areas at the slope toe were assigned the Topsoil category, as illustrated in Figure 4.

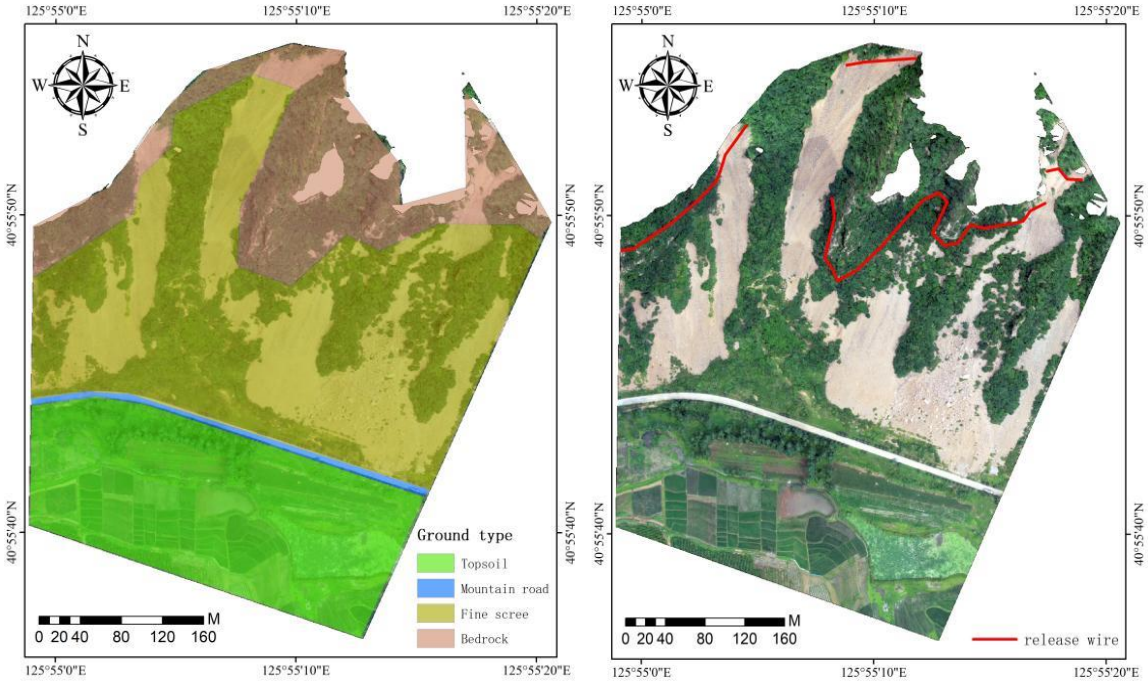


**Figure 4:** Ground type classification map and release location diagram

To accurately reflect the grain-size distribution characteristics of rockfalls within the study area, five pre-established size classes of rockfall models were released from each designated release point in a quantitative ratio of 3:3:2:1:1, resulting in a total of 100 rockfall samples per simulation. This ratio configuration was meticulously designed by integrating the statistical grain-size distribution of historical rockfall events with the discontinuity cutting patterns of unstable rock masses. This approach ensures that the high-frequency occurrence of small-diameter rock blocks is adequately represented while simultaneously accounting for the significant hazard threats posed by larger-scale rock masses.

To fully incorporate stochastic factors during the kinematic evolution of rockfalls, the Monte Carlo method was implemented across multiple simulation iterations. In each simulation run, the initial orientations (rotational angles) and

minor spatial perturbations of the release positions for each rock block were generated via random distributions. This methodology effectively replicates the random nature of rock mass instability encountered in actual collapse events. Through the iterative release of these 100 rockfall samples, a total of 129,000 independent rockfall trajectories were generated. This substantial dataset provides a robust statistical foundation for subsequent analysis of dynamic parameters and the systematic assessment of rockfall hazards.

### 4.4 Feature Extraction and Analysis of Rockfall Movement

Rockfall motion frequency, defined as the cumulative number of rockfall passages within a unit grid, serves as an essential metric reflecting the spatial concentration of trajectories and the intensity of the hazard. High-frequency zones signify a pronounced convergence of rockfall paths, where the terrain is subjected to frequent impacts and elevated disaster threat levels. Consequently, these areas represent critical target locations for the strategic deployment of protection engineering.

The simulation results, illustrated in Figure 5, reveal a pronounced spatial heterogeneity in rockfall frequency, with cumulative values ranging from 0 to 254 passages per grid cell. To effectively delineate the hazard intensity across the terrain, these frequencies are systematically classified into five distinct intervals, each associated with a specific color-coded hazard level. Specifically, the low-frequency zone comprises 0 to 23 passages (dark green), while the medium-low and medium-frequency zones are demarcated by ranges of 23 to 63 (yellow-green) and 63 to 116 (yellow), respectively. As the trajectory convergence intensifies, the medium-high frequency zone is defined by 116 to 179 passages (orange), culminating in the high-frequency zone (179 to 254 passages, red). These high-frequency areas identify the primary corridors of rockfall activity and represent the most critical zones where the probability of impact is maximized, thereby providing a preliminary spatial basis for the subsequent optimization of protective structures.

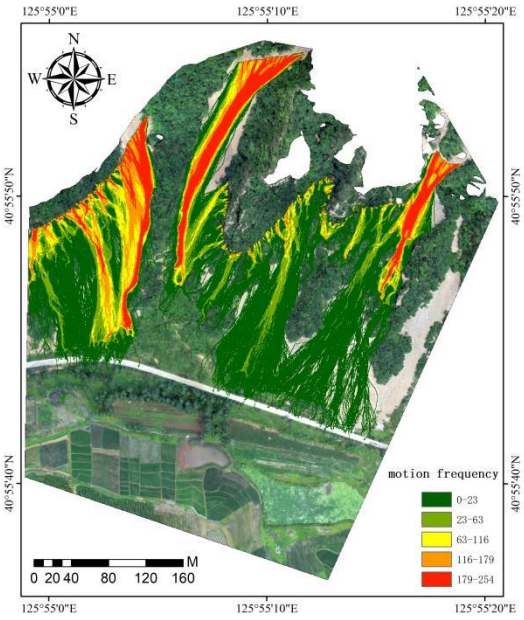


**Figure 5:** Spatial distribution of rockfall frequency

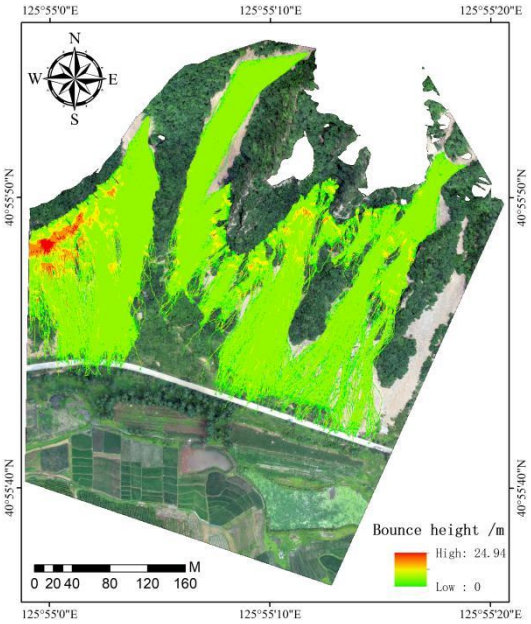


**Figure 6:** Spatial distribution of rockfall bounce height

During rockfall motion, the bounce height is defined as the vertical distance between the moving rock block and the slope surface directly beneath it. It serves as a critical kinematic parameter for evaluating both the energy evolution and the hazard intensity of rockfall events. Based on the data extracted from RAMMS simulations, the bounce height characteristics within the study area were comprehensively analyzed through a combination of global spatial distribution and localized profile assessments at the slope toe. As illustrated in the regional distribution map (Figure 5), the bounce height ranges from 0 to 24.94 m, exhibiting pronounced spatial heterogeneity.

Generally, the high-value zones of bounce height are characterized by a discontinuous, patchy distribution. This spatial pattern is intrinsically consistent with the intermittent nature of rockfall kinematics, where rock blocks undergo successive cycles of "free fall—impact—rebound—descent." The magnitude of each bounce is governed by a complex interplay of stochastic factors, including the local micro-topography at the impact point, the orientation of the rock mass, and the incident angle. Consequently, these dynamics manifest as significant spatial non-uniformity across the slope surface.

To further quantify the specific threats posed to the transportation infrastructure at the slope toe, a representative longitudinal profile was established along the adjacent highway (Figure 6). This profile, extending approximately 400 m, captures the variation in rockfall bounce heights at different positions along the vulnerable road segment. A specialized statistical analysis of the 1,322 valid data points recorded along this corridor (Figure 7) revealed that bounce heights range from 0.25 to 4.94 m, with a mean value of 1.18 m and a median of 1.1 m (standard deviation = 0.50 m). The overall dataset exhibits a characteristically right-skewed distribution, indicating that while most rockfalls maintain a relatively low bounce height near the road, the potential for high-clearance impacts remains a critical factor for the design of passive protection systems.

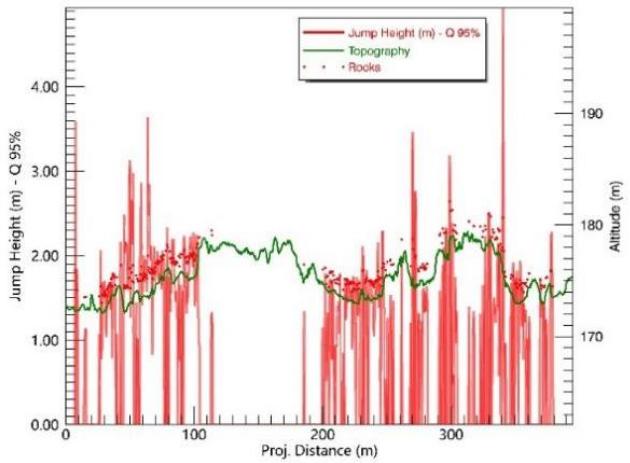


**Figure 6:** Profile of rockfall bounce height

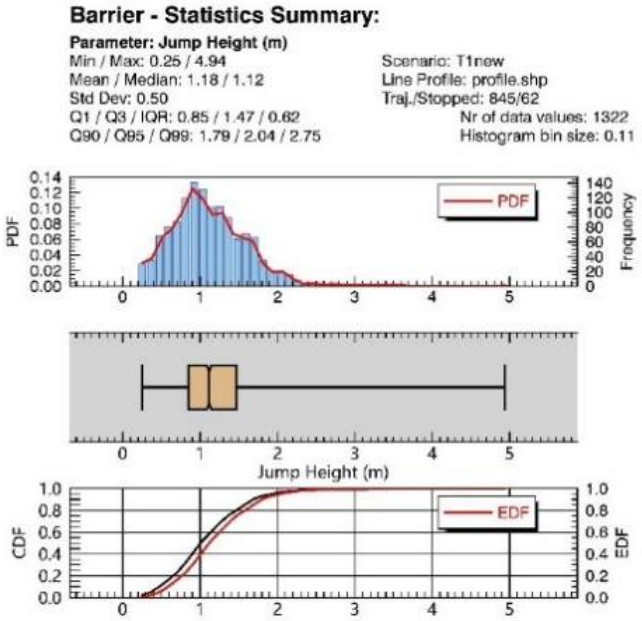


**Figure 7:** Statistical distribution

Rockfall velocity is a fundamental parameter that characterizes both the kinetic energy and the destructive impact potential of rock mass movements. By integrating velocity data derived from RAMMS numerical simulations with comprehensive spatial distribution and slope-toe profile analyses, the evolutionary characteristics of rockfall velocity and their subsequent implications for protection design can be rigorously evaluated. As illustrated in the three-dimensional velocity distribution map (Figure 8), magnitudes range from 0 to 31.21 m/s, exhibiting a pronounced spatial gradient.

Macroscopically, the velocity field displays a distinct spatial transition, characterized by a gradient from high-velocity regimes on the steep source cliffs to moderate speeds across the slope surface, and eventually decelerating to lower velocities at the slope toe. In contrast to the patchy and discrete distribution observed in the bounce height analysis, the high-velocity zones demonstrate greater spatial continuity and concentration. These velocities form ribbon-like corridors aligned with the primary rockfall pathways, reflecting the directional acceleration of rock masses driven by gravity along the terrain's principal fall lines.

A refined statistical assessment of the 1,322 valid data points recorded along the highway corridor (Figure 9) indicates that velocities vary between 0.02 and 15.5 m/s, with a mean of 3.85 m/s and a median of 3.09 m/s (standard deviation = 2.86 m/s). The overall dataset is markedly right-skewed, suggesting that while the majority of rockfalls reach the road at moderate speeds, the potential for high-velocity impacts remains a significant design consideration.

The longitudinal velocity profile established along the highway alignment (Figure 10) further elucidates complex spatial fluctuations in impact intensity. In the western section, velocities exhibit intense fluctuations; the 95th percentile (Q95%) velocity histogram shows concentrations between 12 and 1 m/s, with local peaks approaching 1 m/s. The vertical displacement between the rockfall scatter points and the topographic line indicates that motion in this segment is dominated by high-velocity bouncing, confirming that this section lies within a primary motion corridor characterized by high-energy impact intensity.

While the middle section displays a moderate decline in velocity—with most values maintained between 8 and 15 m/s and a sparse distribution—the eastern section shows a resurgent increase in velocity. In this latter segment, velocities predominantly range from 10 to 20 m/s, with local maxima exceeding 20 m/s. The significant elevation of several red scatter points above the terrain line implies that rock masses traverse this section in a state of high-velocity flight or bounce. Such high-speed trajectories indicate that rockfalls possess the potential to bypass the roadway entirely, posing a direct threat to the infrastructure and the areas situated further down slope.

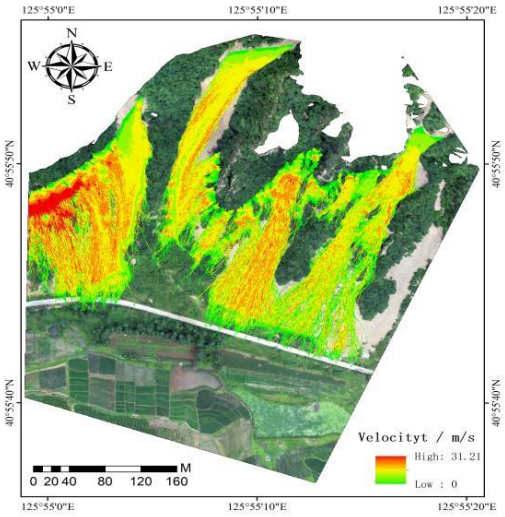


**Figure 8:** Spatial distribution of rockfall velocity

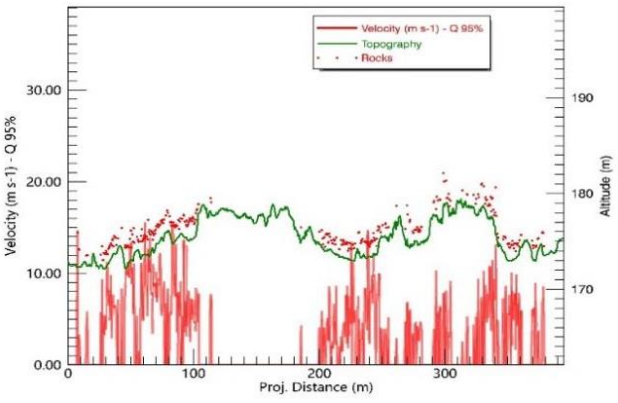


**Figure 9:** Velocity profile along the slope toe

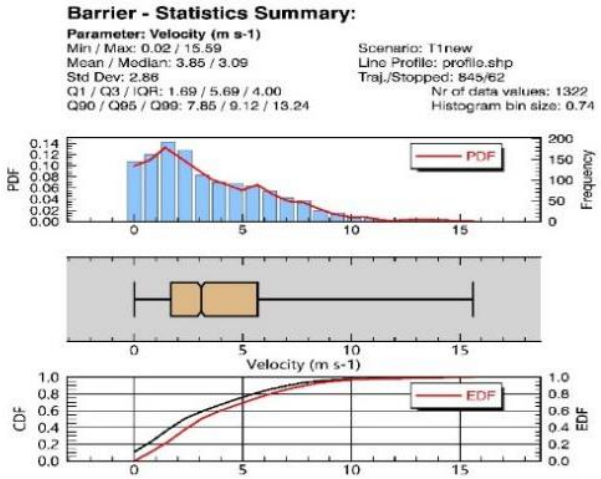


**Figure 10:** Statistical distribution

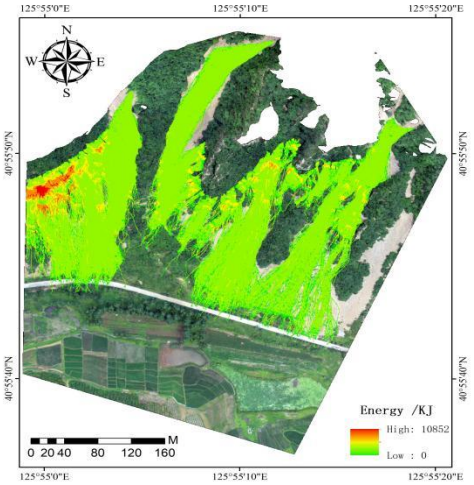


**Figure 11:** Spatial distribution of rockfall kinetic energy

Rockfall kinetic energy serves as the primary determinant for protection engineering design, as it directly dictates the requisite energy-rating selection for protective structures. By integrating kinetic energy data derived from RAMMS numerical simulations with comprehensive spatial distribution patterns and localized slope-toe profile analyses, a quantitative framework is established for the selection and deployment of protective measures. As illustrated in the three-dimensional spatial distribution map (Figure 11), the kinetic energy ranges from 0 to 10,852 kJ, exhibiting pronounced spatial gradients and distinct topographic channeling features.

Rockfall kinetic energy serves as the primary determinant for protection engineering design, as it directly dictates the requisite energy-rating selection for protective structures. By integrating kinetic energy data derived from RAMMS numerical simulations with comprehensive spatial distribution patterns and localized slope-toe profile analyses, a quantitative framework is established for the selection and deployment of protective measures. As illustrated in the three-dimensional spatial distribution map (Figure 11), the kinetic energy ranges from 0 to 10,852 kJ, exhibiting pronounced spatial gradients and distinct topographic channeling features.

Macroscopically, the energy field follows a clear spatial gradient transition: high-energy concentrations are primarily situated at the source cliffs, followed by moderate-to-high energy diffusion across the slope, and ultimately decelerating to moderate-to-low energy levels at the slope toe. Compared to the velocity distribution, the high-energy zones are significantly more localized and exhibit a much broader numerical span. This phenomenon reflects the compounded effect of rock mass disparities and velocity fluctuations, providing a scientific rationale for implementing hierarchical fortification strategies across the site.

The longitudinal kinetic energy profile established along the highway alignment (Figure 12) reveals intense spatial fluctuations in impact intensity. A refined statistical analysis of the 1,322 valid data points within the roadside corridor (Figure 13) indicates a kinetic energy range of 0 to 3,195.2 kJ, with a mean of 262.01 kJ and a median of 90.74 kJ (standard deviation = 421.14 kJ). The overall dataset displays a characteristically extreme right-skewed distribution, underscoring the dominance of low-to-moderate energy events punctuated by high-magnitude impacts.

The profile analysis further highlights the significant non-uniformity of energy distribution along the roadway. Specifically, the western and eastern segments are identified as high-energy threat zones, where the 95th percentile (Q_95%) kinetic energy values range between 1,000 and 3,000 kJ. In contrast, the middle section is characterized as a relatively low-energy zone, with Q_95% values remaining below 500 kJ. This spatial divergence underscores the channeling characteristics of rockfall trajectories and provides a robust empirical basis for the sectional design and energy-level optimization of protection systems.

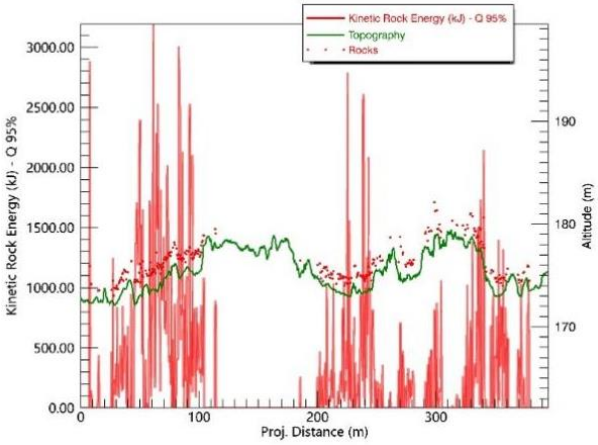


**Figure 12:** Kinetic energy profile along the slope toe

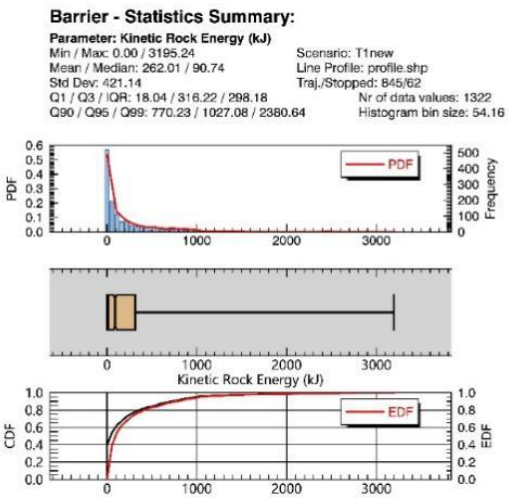


**Figure 13:** Statistical distribution

To quantitatively evaluate the spatial distribution of rockfall hazards in the Guanmenla area, this study implemented a multi-factor weighted superposition method for hazard zonation, utilizing kinematic parameters derived from RAMMS numerical simulations. Based on the disaster-causing mechanisms of rockfall events, three key parameters—rockfall frequency, bounce height, and kinetic energy—were selected as the primary hazard evaluation indicators. Specifically, frequency represents the probability of occurrence, bounce height reflects the kinematic state of the rock masses, and kinetic energy quantifies their destructive potential. Drawing upon the hazard evaluation framework of the Rockfall Analysis software, the weighting coefficients were assigned as 0.5 for frequency, 0.2 for bounce height, and 0.3 for kinetic energy. The resulting hazard zonation is illustrated in Figure 14.

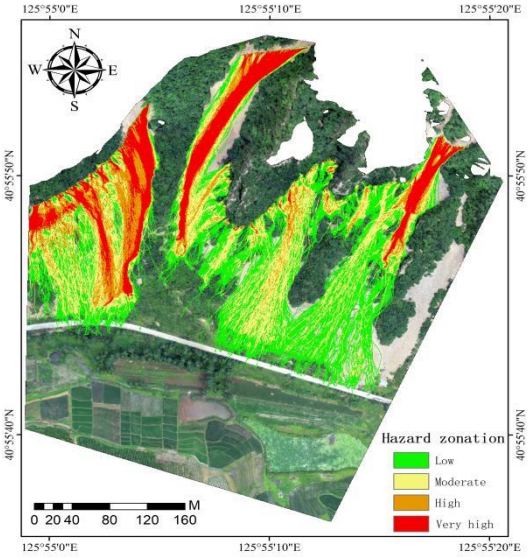


**Figure 14:** Spatial zonation of rockfall hazards in the study area

The results demonstrate that very high hazard zones are primarily concentrated across the upper and central portions of the cliff's western and northeastern sectors, exhibiting a distinct ribbon-like distribution pattern. These areas correspond to the primary rockfall motion corridors, representing core threat zones where frequency, bounce height, and kinetic energy simultaneously attain maximum values. Notably, the very high hazard zone on the western side of the cliff extends directly to the slope toe, forming a continuous high-risk conduit that poses an immediate threat to the underlying roadway and residential areas. Although the very high hazard zone on the northeastern side is relatively smaller in area, it exhibits similar characteristics of high frequency and high energy intensity. The formation of these zones is predominantly governed by steep topographic gradients, highly fragmented rock mass structures, and directional acceleration driven by gravity. High hazard zones are distributed peripherally to the very high hazard areas, maintaining close connectivity and displaying a fan-shaped outward diffusion. These zones correspond to the margins of the primary motion paths and secondary motion corridors; despite a localized reduction in certain kinematic parameters, the integrated hazard level remains substantial. Large-scale high hazard zones are present on both the western side and the center of the cliff, indicating a degree of trajectory divergence in the rockfall motion. Moderate hazard zones are extensively distributed across the middle and lower slopes, appearing in broad, sheet-like patterns. While the overall rockfall threat is attenuated in these regions, localized high-risk points may still emerge in areas characterized by significant topographic relief or abrupt changes in slope gradient. It is noteworthy that the central portion of the residential area at the slope toe falls within the moderate hazard zone, with houses situated near the eastern side of the cliff particularly exposed to significant rockfall risk. Finally, low hazard zones are predominantly located at the margins of the impact area and in regions far removed from the primary motion corridors. Although the probability of direct impact is relatively low in these zones, the possibility of isolated high-velocity rockfalls reaching these locations under extreme conditions cannot be entirely discounted.

### 4.5 Verification and Evaluation of Optimization Schemes

Based on the RAMMS numerical simulation results, a multi-objective optimization model for the layout of passive flexible protection networks was established. Following the hazard zonation analysis, the threatened road segments were categorized into four critical protection sector (M1, M2, M3, M4). For each sector, the decision variables included the network height $h_i \in [3.0,6.0]$ m, energy capacity $C_i \in \{1500,2000,3000,4000,5000\}$ kJ, network length $L_i$ and the specific placement orientation.

The objective functions of the optimization model were formulated to maximize the interception efficiency while simultaneously minimizing the total economic expenditure:

$$maxR = \frac{N_{intercepted}}{N_{total}} \times 100\%$$

$$minC_{total} = \sum_{i=1}^{n} (C_{unit,i} \cdot L_i + C_{install,i})$$

Where $R$ denotes the interception rate, $N_{intercepted}$ is the number of successfully intercepted rockfalls, $N_{total}$ is the total number of simulated samples. $C_{total}$ represents the cumulative project cost, $C_{unit}$ is the unit material cost per meter, which fluctuates between 1,200 and 2,500 RMB/m depending on the required energy rating.

To ensure the structural integrity and functional reliability of the proposed mitigation measures, the optimization process was governed by several rigorous engineering constraints. Primarily, the design height of each flexible network was required to be no less than the 95th percentile bounce height of 2.04m recorded at its respective deployment location. Furthermore, the energy-absorption capacity of each structure was mandated to meet or exceed the local 95th percentile kinetic energy to prevent structural failure upon impact. Additionally, the longitudinal spacing and alignment between adjacent networks were meticulously configured to comply with the relevant technical codes and design specifications for rockfall protection engineering.

The multi-objective optimization problem was solved using the NSGA-II algorithm, which achieved computational convergence at the 265th generation. The resulting optimal layout adopts a zonal cascading protection strategy, incorporating a total of four flexible protection networks strategically positioned across the high-risk corridors. This integrated configuration achieves a high level of disaster

resilience, providing a total interception rate of 98.43%. The overall engineering cost for the proposed scheme is estimated at 368,440 RMB, demonstrating an efficient balance between safety performance and economic investment as detailed in Table 4.

**Table 4:** Optimized design parameters and performance metrics of the protection system

| Net ID | Sector Group | Heigh t (m) | Energy Capacity (kJ) | Length (m) | Sector Interception (%) |
|---|---|---|---|---|---|
| M1 | Group 1 | 5.0 | 5000 | 120.3 | 96.6 |
| M2 | Group 1 | 4.9 | 4402 | 140.9 | |
| M3 | Group 2 | 3.6 | 3252 | 194.9 | 99.8 |
| M4 | Group 2 | 3.8 | 3923 | 170.8 | |
| Total | | | | | 98.43 |

The interception efficiency of the optimized scheme across the four designated protection sectors is illustrated in Figure 15. The individual interception rates for sectors M1 through M4 were determined to be 94.6%, 71.9%, 94.3%, and 83.9%, respectively. These performance variations are primarily governed by the localized interplay of rockfall frequency, energy distribution, and topographic constraints within each sector. To achieve an optimal allocation of resources, the scheme deploys high-energy dense protection in the northwestern high-risk sectors (M1–M2), while a medium-energy cascading strategy is implemented for the southeastern moderate-to-high risk sectors (M3–M4).

The final configuration is organized into two distinct cascading protection systems. The first group (M2 → M1) specifically targets the primary western rockfall corridor, achieving a combined interception rate of 96.6% with a total investment of 191,030 RMB. In this system, network M2 is configured with a height of 5.0 m, an energy capacity of 5,000 kJ, and a length of 120.3 m, while M1 serves as a downstream barrier with a height of 4.9 m, an energy capacity of 4,402 kJ, and a length of 140.9 m. This high-energy specification is necessitated by the extreme kinetic energy recorded in the western corridor, where the 95th percentile values reach 3,200 kJ.

The second group (M4–M3) addresses the southeastern secondary corridor, yielding a superior combined interception rate of 99.8% at a cost of 177,41 RMB. The parameters for M4 include a height of 3.2 m, an energy capacity of 3,362 kJ, and a length of 194.9 m, complemented by M3 with a height of 3.8 m, an energy capacity of 3,923 kJ, and a length of 170.8 m. The significantly higher interception efficiency of this second group is attributed to the smaller rockfall grain sizes, lower kinetic energies, and more favorable topographic conditions characteristic of the southeastern slope.

Regarding the spatial arrangement, networks M1 and M2 are strategically positioned within the northwestern high-risk zone to establish a robust defense-in-depth. Conversely, M3 and M4 are deployed in the southeastern sector, following the topographic contours in a curvilinear, arched distribution. All four flexible networks are located within high or very high hazard zones, strictly adhering to the design principle of "prioritized protection with a sparse-to-dense upslope-downslope gradient." This contour-aligned placement maximizes the effective interception area and ensures a more uniform distribution of impact forces across the structural components, thereby facilitating both construction feasibility and long-term maintenance.

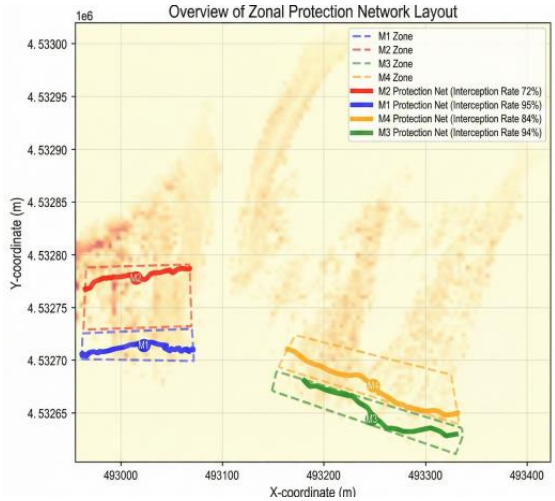


**Figure 15:** Layout of the optimized protection scheme

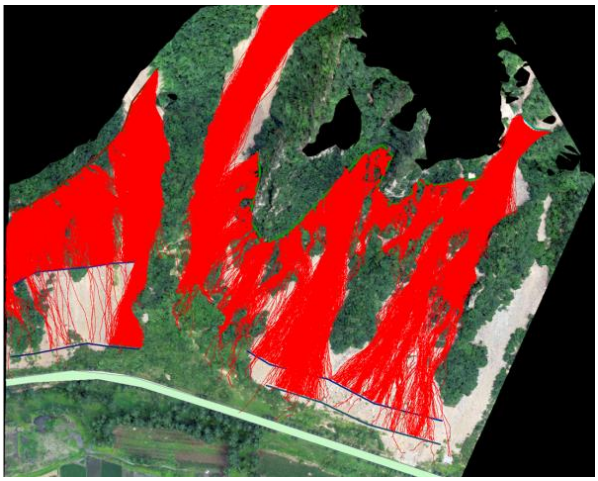

**Figure 16:** Back-verification results in RAMMS

To validate the predictive accuracy and engineering reliability of the proposed model, the optimized design parameters were re-integrated into the RAMMS platform for comprehensive back-verification. Within this simulation environment, the protection networks were modeled as flexible barriers endowed with specific energy-absorption characteristics. The interception outcomes were determined by the mechanical relationship between the rockfall's impact kinetic energy and the designated energy capacity of the protective structure. The verification results yielded an actual interception rate of 98.43%, demonstrating a high degree of congruence with the optimization framework's predicted values, with a relative error of less than 0.5%.

A detailed statistical analysis of the penetrating rock masses was conducted to elucidate the limitations of the protective system. The findings indicate that the majority of non-intercepted rocks (85%) belonged to the minimum size class (21.5 kg), while 10% and 5% were categorized into the second-smallest and medium size classes, respectively. Notably, the kinetic energy of all penetrating rocks remained below 200 kJ, significantly lower than the design thresholds of the barriers. Spatially, the trajectories of these penetrating masses were primarily concentrated at the lateral boundaries of the protection networks and within the transition zones between the two primary functional groups.

## 5. Conclusions

Taking the Guanmenla rockfall area in Ji'an City, Jilin Province, as a case study, this research establishes a design framework for passive flexible protection network layout by coupling three-dimensional numerical simulation with a multi-objective optimization algorithm. By integrating RAMMS-based rockfall motion analysis with the NSGA-II optimization algorithm, an effective equilibrium between interception efficiency and engineering cost is achieved. Based on a 0.5 m resolution DEM and 129,000 Monte Carlo simulations, the statistical distribution of rockfall dynamics was characterized. The 95th percentile values for jump height and velocity along the road were determined to be 2.04 m and 9.12 m/s, respectively, while the 95th percentile kinetic energy reached 3,200 kJ in the western section and ranged from 500 to 2,800 kJ in the eastern section. Through a multi-factor weighted evaluation integrating frequency, jump height, and kinetic energy, two primary rockfall channels on the western and northeastern slopes were quantitatively identified, providing a rigorous basis for protection deployment.

The developed multi-objective optimization model, which seeks to maximize interception rates while minimizing costs, reached convergence at the 265th generation using the NSGA-II algorithm. The resulting optimal scheme consists of four protection networks with a total interception rate of 98.43% and a total engineering cost of 368,440 RMB. Specifically, high-energy networks (4,402–5,000 kJ) are deployed for intensive protection in the northwestern high-risk zone, while medium-energy networks (3,362–3,923 kJ) provide extended coverage in the southeastern medium-to-high-risk zone. Back-verification using RAMMS demonstrates that the error between optimization predictions and actual simulation values is less than 0.5%. Compared to traditional empirical methods, this framework ensures a more objective selection of protection measures, significantly reducing costs while maintaining a high level of interception efficiency.

## References


[1] Caviezel, A., Ringenbach, A., Demmel, S. E., Dinneen, C. E., Krebs, N., Bühler, Y., Christen, M., Meyrat, G., Stoffel, A., Hafner, E., Eberhard, L. A., Rickenbach, D. V., Simmler, K., Mayer, P., Niklaus, P. S., Birchler, T., Aebi, T., Cavigelli, L., Schaffner, M., … Bartelt, P. (2021). The relevance of rock shape over mass—Implications for rockfall hazard assessments. *Nature Communications*, 12(1), 5546. https://doi.org/10.1038/s41467-021-25794-y

[2] *Development of Parallel Multiobjective Genetic algorithm for Designing Flexible Systems-All Databases*. (n.d.). Retrieved December 23, 2025, from https://webofscience.clarivate.cn/wos/alldb/full-record/GRANTS:14309062

[3] Ferrari, F., Giacomini, A., & Thoeni, K. (2016). Qualitative Rockfall Hazard Assessment: A Comprehensive Review of Current Practices. *Rock Mechanics and Rock Engineering, 49*(7), 2865–2922. https://doi.org/10.1007/s00603-016-0918-z

[4] Gottardi, G., & Govoni, L. (2010). Full-scale Modelling of Falling Rock Protection Barriers. *Rock Mechanics and Rock Engineering, 43*(3), 261–274. https://doi.org/10.1007/s00603-009-0046-0

[5] Kumar, S., Sharma, A., & Singh, K. (2024). A Comprehensive Review on Debris Flow Landslide Assessment Using Rapid Mass Movement Simulation (RAMMS). *Geotechnical and Geological Engineering, 42*(7), 5447–5475. https://doi.org/10.1007/s10706 -024-02887-1

[6] Li, F., Torgoev, I., Zaredinov, D., Li, M., Talipov, B., Belousova, A., Kunze, C., & Schneider, P. (2021). Landslide-Induced Mass Transport of Radionuclides along Transboundary Mailuu-Suu River Networks in Central Asia. Remote Sensing, 13(4), 698. https://doi.org/10.3390/rs13040698

[7] Lu, G., Caviezel, A., Christen, M., Demmel, S. E., Ringenbach, A., Bühler, Y., Dinneen, C. E., Gerber, W., & Bartelt, P. (2019). Modelling rockfall impact with scarring in compactable soils. *Landslides, 16*(12), 2353–2367. https://doi.org/10.1007/s10346-019-01238-z

[8] Moral, R. J., & Dulikravich, G. S. (2008). Multi-objective hybrid, evolutionary optimization with automatic switching among constituent algorithms. *Aiaa Journal, 46*(3), 673–681. International Annual Meeting of the American-Association-of-Cereal-Chemists. https://doi.org/10.2514/1.28926

[9] Sarro, R., Mateos, R. M., García-Moreno, I., Herrera, G., Reichenbach, P., Laín, L., & Paredes, C. (2014). The Son Poc rockfall (Mallorca, Spain) on the 6th of March 2013: 3D simulation. *Landslides, 11*(3), 493–503. https://doi.org/10.1007/s10346-014-0487-8

[10] Volkwein, A., Schellenberg, K., Labiouse, V., Agliardi, F., Berger, F., Bourrier, F., Dorren, L. K. A., Gerber, W., & Jaboyedoff, M. (2011). Rockfall characterisation and structural protection—A review. *Natural Hazards and Earth System Sciences, 11*(9), 2617–2651. https://doi.org/10.5194/nhess-11-2617-2011

[11] Yang, H., Xing, B., He, J., Cheng, Q., & Wang, F. (2023). The kinematic characterization of a rockfall in Zagunao Valley in the eastern margin of the Tibetan Plateau. *Landslides, 20*(3), 601–614. https://doi.org/10.1007/s10346-022-02008-0

[12] Yannibelli, V., & Amandi, A. (2013). Hybridizing a multi-objective simulated annealing algorithm with a multi-objective evolutionary algorithm to solve a multi-objective project scheduling problem. *Expert Systems with Applications, 40*(7), 2421–2434. https://doi.org/10.1016/j.eswa.2012.10.058

[13] Yu, B., Chen, F., & Xu, C. (2020). Landslide detection based on contour-based deep learning framework in case of national scale of Nepal in 2015. *Computers & Geosciences*. https://doi.org/10.1016/j.cageo.2019.104388

[14] Zhang, Z., & Lu, B. (2021). Improving NSGA-II by a Local Search Strategy with Gaussian Mutation. In C. Peng & J. Sun (Eds.), *2021 Proceedings of the 40th Chinese Control Conference (ccc)* (pp. 1628–1633). IEEE.

[15] Zhao, F., Huan, L., Zhang, Y., Ma, W., & Zhang, C. (2018). A Novel Multi-Objective Optimization Algorithm Based on Differential Evolution and NSGA-II. In W. Shen, J. Luo, J. P. Barthes, F. Dong, J. Zhang, & H. Zhu (Eds.), *Proceedings of the 2018 Ieee 22nd International Conference on Computer Supported*

*Cooperative Work in Design ((cscwd))* (pp. 570–575). IEEE.

[16] Hu, Y. N., Wang, L. S., Zhao, Q. H., & Xu, J. (1996). Simulation study on rockfall kinematics. Journal of Geological Hazards and Environment Preservation, 2, 25–32. https://kns.cnki.net/KCMS/detail/detail.aspx?dbcode=CJFQ&dbname=CJFD9697&filename=DZHB602.003

[17] Fu, W. (2021). Development characteristics and protection measures of dangerous rockfalls on the Xi'an-Shiyan Railway. Journal of Railway Engineering Society, 38(4), 22–27.

[18] He, S. M., Wang, D. P., Wu, Y., & Ouyang, C. J. (2014). Mechanical mechanism and prevention technology of rockfall hazards. Chinese Journal of Nature, 36(5), 336–345

[19] Liu, H. M. (2012). Study on rockfall trajectory of Longmen Peak in Changbai Mountain Tianchi area [Master's thesis, Jilin University].

[20] Zhou, X. Y., Chen, A. R., & Ma, R. J. (2012). Numerical simulation of energy dissipation law of rockfall flexible protection networks. Journal of Chang'an University (Natural Science Edition), 32(6), 59–66.

[21] Zhang, Y. C. (1993). Basic characteristics and prevention approaches of collapse, landslide, and debris flow disasters in China. Journal of Geological Hazards and Environment Preservation, 1, 11–18

[22] Zhang, C. S., Zhang, Y. C., & Zhang, L. H. (2004). Risk assessment of collapse, landslide, and debris flow disasters in China. Journal of Geomechanics, 1, 27–32.

[23] Zhang, Z. P., Xia, Z. X., Jin, C. R., & Zhao, L. H. (2021). Rockfall path acquisition based on photogrammetry and service performance evaluation of passive protection networks. Chinese Journal of Rock Mechanics and Engineering, 40(S2), 3274–3283

[24] Zhao, S. C., Yu, Z. X., Wei, T., & Qi, X. (2013). Experimental study and numerical calculation of mechanical mechanism of passive flexible protection networks. China Civil Engineering Journal, 46(5), 122–128.

[25] Zhao, L. H., Jin, C. R., Huang, D. L., Zhao, B., Zeng, Z. L., & Hu, S. H. (2023). Study on three-dimensional protection effect evaluation of passive protection networks for dangerous rockfalls in complex terrain. Journal of the China Railway Society, 45(5), 143–150.

[26] Zhong, X. (2021). Study on dynamic response and energy distribution law of rockfall impacting passive protection networks: A case study of Shuangyong Road rockfall control project in Danba County [Master's thesis, Chengdu University of Technology].